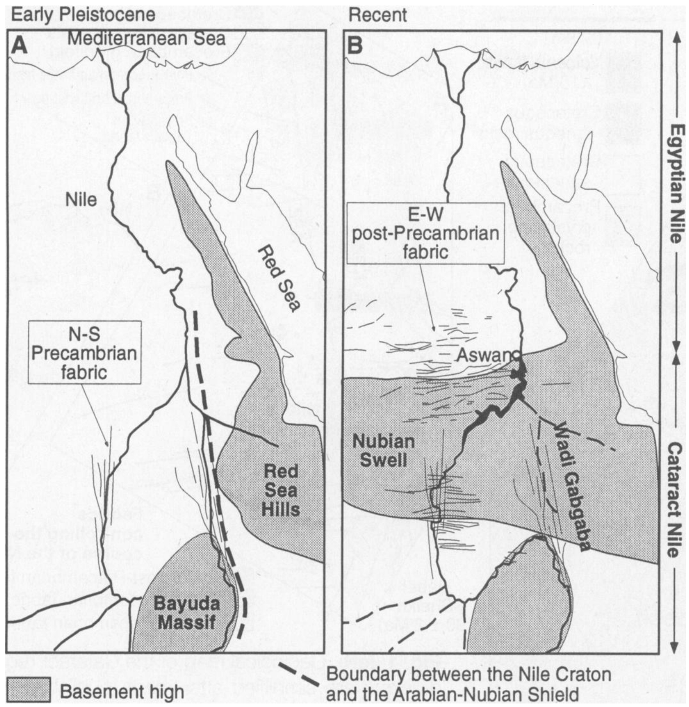


**Fig. 4.** A model explaining the Quaternary evolution of the Nile and the formation of the great bend. (**A**) The Nile in Nubia comprises two north-flowing branches that follow Precambrian fabrics. The main, eastern branch flows along the Late Precambrian suture between the older Nile craton to the west and the juvenile crust of the Arabian-Nubian Shield to the east. The western branch follows a fabric of similar age and orientation. (**B**) Uplift along an E-W axis to form the Nubian Swell diverts the eastern branch of the Nile to flow SW to connect with the western branch of the Nile. Wadi Gabgaba represents the abandoned course of the eastern branch.

imity of the Gabgaba-Nile drainage divide to the Nile (Fig. 1): We suggest that before Nubian Swell uplift, the drainage now flowing along the fifth cataract stretch continued north through what is now Wadi Gabgaba (Fig. 4A). Quaternary uplift diverted the Nile to the west, through the fourth cataract region, perhaps to join a tributary to the west (Fig. 4B), an interpretation that is consistent with the inference that the fourth cataract stretch of the Nile has only been established since the early Pleistocene (*2*). Uplift of the Nubian Swell continued to deflect the Nile to the south along the fourth cataract stretch.

### REFERENCES AND NOTES


1. R. Said, *The Geological Evolution of the River Nile* (Springer-Verlag, New York, 1981).
2. L. Berry and A. J. Whiteman, *Geogr. J.* **134**, 1 (1968).
3. D. Adamson and F. Williams, in *The Sahara and the Nile*, M. A. J. Williams and H. Faure, Eds. (Balkema, Rotterdam, Netherlands, 1980), pp. 225–252.
4. R. L. Jordan, B. L. Huneycutt, M. Werner, *IEEE Trans. Geosci. Remote Sensing* **33**, 829 (1995).
5. The SIR-C/X-SAR radar system has advantages over visible and near-infrared imagery in that radar is sensitive to surface roughness and orientation and has limited capabilities for imaging beneath sand. Hence, the SIR-C/X-SAR imagery is more sensitive to geologic structures and is especially useful in hyperarid and poorly known regions such as the Sahara.
6. K. J. Hsu, W. B. F. Ryan, M. B. Cita, *Nature* **242**, 240 (1973).
7. R. Said, in *The Nile: Sharing a Scarce Resource*, P. P. Howell and J. A. Allan, Eds. (Cambridge Univ. Press, Cambridge, 1994), pp. 17–26.
8. H. G. Lyons, *The Physiography of the River Nile and Its Basin* (Survey Department, Cairo, Egypt, 1906). Lyons relays a report by Ball that the position of flood marks of the XII Dynasty near Semna along the second cataract stretch (now flooded) indicates about 8 m of erosion over the past 4000 years.
9. The Nubian Swell is a region of shallowly buried and exposed basement that extends E-W along the Egypt-Sudan border as far as J. Uweinat, 600 km west of the Nile. Only the eastern part of it is shown in Fig. 1.
10. H. Schandelmeier *et al.*, *Geology* **22**, 563 (1994).
11. U. Harms, D. P. F. Darbyshire, T. Denkler, M. Hengst, H. Schandelmeier, *Geol. Rundsch.* **83**, 591 (1994).
12. M. G. Abdelsalam and R. J. Stern, *J. Geophys. Res.* **101**, 23063 (1996).
13. E. H. Klitzsch and C. H. Squyres, *Am. Assoc. Petrol. Geol. Bull.* **74**, 1203 (1990).
14. G. Franz, U. Harms, T. Denkler, P. Pasteels, in *Geoscientific Research in Northeast Africa*, U. Thorweihe and H. Schandelmeier, Eds. (Balkema, Rotterdam, Netherlands, 1993), pp. 227–230.
15. L. Cahen, N. J. Snelling, J. Delhal, J. R. Vail, *The Geochronology and Evolution of Africa* (Clarendon, Oxford, 1984).
16. R. J. Stern, *Annu. Rev. Earth Planet. Sci.* **22**, 319 (1994).
17. W. Bosworth, *Tectonophysics* **209**, 115 (1992).
18. F. Ahmed, *Adv. Space Res.* **3**, 71 (1983).
19. B. Issawi, *Ann. Geol. Surv. Egypt* **3**, 25 (1973).
20. D. Müller-Sohnius and P. Horn, *Geol. Rundsch.* **83**, 604 (1994).
21. W. F. Hume, *Geology of Egypt, part I, The Metamorphic Rocks* (Government Press, Cairo, Egypt, 1934). Hume's geological reconnaissance of several of the islands in the fourth cataract stretch, which he reached by swimming through the rapids on inflated skins, remains the basis for our geological understanding of this region.
22. K. W. Butzer and C. L. Hansen, *Desert and River in Nubia* (Univ. of Wisconsin Press, Madison, WI, 1968).
23. D. A. Adamson, F. Gasse, F. A. Street, M. A. J. Williams, *Nature* **288**, 50 (1980).
24. M. G. Abdelsalam, R. J. Stern, H. Schandelmeier, M. Sultan, *J. Geol.* **103**, 475 (1995).
25. M. Sultan, R. D. Tucker, Z. El Alfy, R. Attia, A. G. Ragab, *Geol. Rundsch.* **83**, 514 (1994).
26. D. C. Almond, F. Ahmed, B. E. Khalil, *Bull. Volcanol.* **33**, 549 (1969).
27. E. Klitzsch, *Berl. Geowiss. Abh.* **50**, 23 (1984).
28. N. Barazi and J. Kuss, *Geol. Rundsch.* **76**, 529 (1987).


29. We thank the Geological Research Authority of the Sudan for their help, D. Amesbury for bringing our attention to the shuttle photograph of the fourth cataract stretch, and K. Burke and W. Bosworth for their ideas on the problem. Supported by NASA through subcontracts from the Jet Propulsion Laboratory. This is University of Texas at Dallas Programs in Geosciences Contribution 846.

30 July 1996; accepted 18 September 1996


# Interplane Tunneling Magnetoresistance in a Layered Manganite Crystal


T. Kimura, Y. Tomioka, H. Kuwahara, A. Asamitsu, M. Tamura, Y. Tokura



The current-perpendicular-to-plane magnetoresistance (CPP-MR) has been investigated for the layered manganite, $La_{2-2x}Sr_{1+2x}Mn_2O_7$ ($x = 0.3$), which is composed of the ferromagnetic-metallic $MnO_2$ bilayers separated by nonmagnetic insulating block layers. The CPP-MR is extremely large ($10^4$ percent at 50 kilo-oersted) at temperatures near above the three-dimensional ordering temperature ($T_c \approx 90$ kelvin) because of the field-induced coherent motion between planes of the spin-polarized electrons. Below $T_c$, the interplane magnetic domain boundary on the insulating block layer serves as the charge-transport barrier, but it can be removed by a low saturation field, which gives rise to the low-field tunneling MR as large as 240 percent.


The discovery of the giant magnetoresistance (GMR) in magnetic multilayers (*1*) has stimulated much interest in relating spin polarization–dependent transport phenomena from the viewpoints of both the underlying physics and their immediate application to magnetic storage and sensor technology. A variety of the GMR structures have so far been investigated, such as antiferromagnetically coupled multilayers (*2*), granular films (*3*), spin valve (*4*), and tunneling structures (*5*). In these structures, the effects of spin-dependent electron scattering have been assigned to the fundamen-

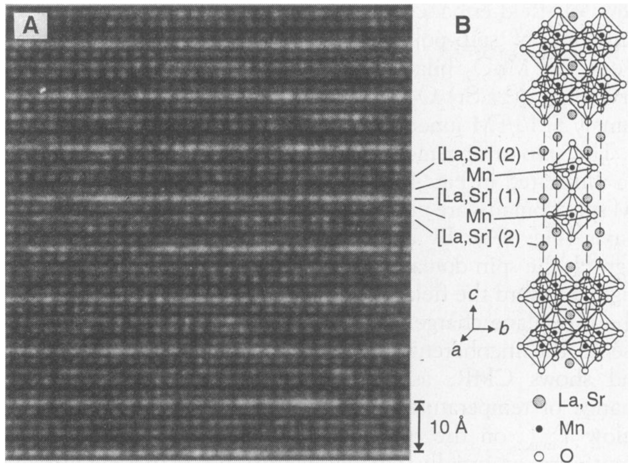


**Fig. 1.** (**A**) An HRTEM lattice image along a [110] zone axis (left). (**B**) The crystal structure of $La_{2-2x}Sr_{1+2x}Mn_2O_7$. The rectangular parallelepiped surrounded by broken lines indicates the unit cell. Shaded planes represent FM-metallic $MnO_2$ planes.

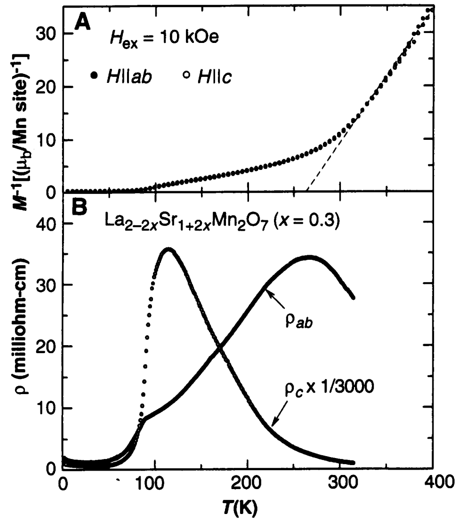


**Fig. 2.** Temperature dependence of (**A**) $M^{-1}$ measured at a field of 10 kOe and (**B**) in-plane ($\rho_{ab}$) and interplane ($\rho_c$) resistivity at zero field in the $La_{2-2x}Sr_{1+2x}Mn_2O_7$ ($x = 0.3$) crystal.

tal mechanisms for the observed phenomena. Recently, even greater MR, or so-called "colossal magnetoresistance" (CMR), has been observed for perovskite manganites $RE_{1-x}AE_xMnO_3$ (RE and AE being trivalent rare earth and divalent alkaline earth ions, respectively) (6). Perovskite manganites exhibit CMR in the vicinity of a ferromagnetic (FM) ordering temperature of manganese spin, which is explained in terms of field suppression of the spin-dependent scattering of charge carriers (7). The CMR effect in manganites requires a much larger applied magnetic field $H$ than that needed in the artificial magnetic multilayers, although the driving field of CMR effect in manganites has been successfully lowered to some extent by using striction-coupled MR phenomena (8).

In this report, we present observations of the spin-polarized tunneling MR with the current direction perpendicular to the $MnO_2$ sheets in a bulk crystal of layered manganite, $La_{2-2x}Sr_{1+2x}Mn_2O_7$. This system intrinsically includes the magnetic multilayers in its crystal structure (Fig. 1B). The simplest view of the layered manganite is a stack of FM-metallic sheets consisting of the $MnO_2$ bilayers that are respectively separated by the $(La,Sr)_2O_2$ layers, which act as a nonmagnetic insulating barrier (I). In other words, the layered manganite crystal forms a virtually infinite array of FM/I/FM junctions (9). In this simple view, the current perpendicular to the bilayer plane (CPP) carried by the nearly fully spin-polarized electrons encounters the tunneling junctions and responds to $H$. Below the critical temperature $T_c$, where electrons are almost fully polarized, the decrease of domain boundary scattering is responsible for the low-field CPP-MR effect. In contrast, at temperatures just above $T_c$ the extremely large CPP-MR is attributed to the incoherent-coherent transition induced by $H$.

T. Kimura, Y. Tomioka, H. Kuwahara, A. Asamitsu, M. Tamura, Joint Research Center for Atom Technology (JRCAT), Tsukuba, 305, Japan.
Y. Tokura, JRCAT, Tsukuba, 305, Japan, and Department of Applied Physics, University of Tokyo, Tokyo 113, Japan.

Single crystals of $La_{2-2x}Sr_{1+2x}Mn_2O_7$ were grown by the floating-zone method (10). The nominal hole concentration could be lowered to $x = 0.30$, away from the well-known $x = 1/2$ charge-ordering instability (8, 10, 11). Our single-phase samples exhibited the 327 structure with a nearly stoichiometric composition, as confirmed by x-ray diffraction and inductively coupled plasma atomic emission (ICP) spectroscopy. Lattice parameters of the tetragonal unit cell are $a_0 = 3.86$ Å and $c_0 = 20.35$ Å at room temperature. In the [110] image of the grown crystal by high-resolution transmission electron microscopy (HRTEM) (Fig. 1A), the rows of the brightest dots are related to the (La,Sr)O layers sandwiched with $MnO_2$ layers. The resistivity with the current parallel ($\rho_{ab}$) and perpendicular ($\rho_c$) to the $MnO_2$ bilayers was usually measured with the standard four-terminal method [for $\rho_c$ in a thin plate-like crystal ($c < 0.1$ mm), the ring-geometric contacts was also used]. High-quality contacts of low resistance were made by silver paste with a heat treatment.

The temperature profile of $\rho_c$ (Fig. 2B) reveals a sharp maximum at $T^c_{max} \approx 100$ K, with a semiconducting $T$ dependence above $T^c_{max}$ and a metallic-like behavior below $T^c_{max}$. Compared with the magnetization ($M$) data (Fig. 2A), the steep drop of $\rho_c$ below $T^c_{max}$ has an intimate connection to the three-dimensional (3D) spin ordering. This 3D ordering takes place around $T_c \approx$ 90 K with the easy axis along the $c$ axis. The observed saturated moment (3.5 $\mu_B$) is near that expected for the full Mn moment, ensuring the almost 100% spin polarization of the conduction electron due to the large Hund's-rule coupling energy (12). In contrast, $\rho_{ab}$ shows a broad maximum at $T^c_{max} \approx$ 270 K where the slope of $M^{-1}$ changes with departure from the Curie-Weiss law (a dashed line in Fig. 2A). This result implies that the in-plane 2D FM correlation evolves with decrease of $T$ below $T^{ab}_{max}$ that is far above $T^c_{max}$ (or the 3D ordering temperature $T_c$).

At temperatures between $T^c_{max}$ and $T^{ab}_{max}$, $\rho_{ab}$ shows a metallic $T$ dependence in contrast to a semiconducting $\rho_c$. The anisotropy of resistivity ($\rho_c/\rho_{ab}$) is readily as large as $\sim 10^3$ at room temperature, yet increases further between $T^c_{max}$ and $T^{ab}_{max}$ and reaches values as large as $10^4$ at $T^c_{max}$. The remarkable difference between the $T$ dependence of $\rho_{ab}$ and $\rho_c$ is rarely encountered, even among highly anisotropic electronic systems, except for superconducting $Sr_2RuO_4$ (13) and high-$T_c$ cuprates (14). For the present layered manganite, for $T^c_{max} \le T \le T^{ab}_{max}$, the system behaves like a 2D FM metal. Below $T^c_{max}$, the spin correlation extends over the adjacent $MnO_2$ bilayers. The difference between $T^{ab}_{max}$ and $T^c_{max}$ may reflect the difference between the in-plane exchange interaction $J^{ab}$ and the interplane interaction $J^c$. A recent neutron-scattering experiment (15) indicates that $J^c$ is much weaker than $J^{ab}$, perhaps by more than an order of magnitude.

The metallic regime in $\rho_{ab}$ and the strong $T$ dependence of $\rho_c/\rho_{ab}$ at $T^c_{max} \le T \le T^{ab}_{max}$ have not been observed so far for any manganite crystals and is also contrasted by the result of the previous work on the $x = 0.4$ bilayered manganite crystal (10). In the $x = 0.4$ crystal, both $\rho_{ab}$ and $\rho_c$ show a steep increase toward $T_c$ with a large activation energy (30 to 40 meV). The insulating behavior of $\rho_{ab}$ above $T_c$ has been attributed to localization effect due to strong in-plane antiferromagnetic (AF) correlation, which was observed above $T_c$ by a recent study of inelastic neutron scattering (*15*). Such a competition between the double-exchange FM and AF interactions has frequently been observed also in pseudocubic perovskite manganites, which show in general extremely large negative MR at $T$'s immediately above $T_c$ because of the field suppression of AF fluctuation (*8*). The presently observed CPP-MR phenomena are totally different in nature from the previously observed ones, as shown below.

In Fig. 3, we present the effect of $H$ on $\rho_{ab}$ and $\rho_c$. The MR in $\rho_{ab}$ and $\rho_c$ both depends weakly on the relative orientation of the field. The MR in $\rho_{ab}$ is enhanced in the vicinity of the both $T^{ab}_{max}$ and $T^{c}_{max}$ (Fig. 3A). A more remarkable MR effect can be observed for the interplane component (Fig. 3B). $T^{c}_{max}$ is apparently shifted to higher $T$ with increasing $H$, and the resistivity value at $T^{c}_{max}$ is also remarkably reduced. Another important feature is seen in the anisotropic low-field MR effects shown in the respective insets. Below $T^{c}_{max}$, a nearly $T$-independent MR observed with current along the $c$ axis remains quite appreciable even at 10 kOe (it saturates at higher field). In contrast, MR in $\rho_{ab}$ is much smaller than that in $\rho_c$. These observations on the interplane MR are consistent with the view of field-enhanced or field-restored tunneling of spin-polarized electrons between FM $MnO_2$ bilayers through the intervening $(La,Sr)_2O_2$ blocking layers, namely FM/I/FM junctions.

The spin arrangements for this concept are illustrated in Fig. 4. For $T > T^{c}_{max}$, the FM spin domains are uncorrelated along the $c$ axis (Fig. 4A). By applying a relatively high $H$, the spin domains are preferentially aligned toward the field direction (Fig. 4B). The interplane charge transport then gives rise to the incoherent-coherent transition and shows CMR, as evidenced by the change of temperature gradient of $\rho_c$. Far below $T^{c}_{max}$, on the other hand, FM moments are essentially parallel within domains separated by domain boundaries lying on the $(La,Sr)_2O_2$ layers (Fig. 4C). The domain boundary on the $(La,Sr)_2O_2$ layer blocks the interplane tunneling of the spin-polarized electrons. For $H > H_{sat}$, the domains are aligned. With removal of the domain boundaries, the barriers to interplane tunneling disappear (Fig. 4D).

To verify the character of the MR effect, we display in Fig. 5 the isothermal in-plane and interplane MR and M curves at characteristic $T$'s; near $T^{ab}_{max}$ (273 K), $T^{c}_{max}$ (100 K) and at a enough low temperature (4.2 K) to represent the 3D ordering state with nearly full spin polarization. Magnetic fields were applied along the $c$ axis. The magnitude of the MR is correlated with that of M. At 273 K, appreciable negative MR was observed in both $\rho_{ab}$ and $\rho_c$. The magnitude of MR is nearly independent of the current direction. This negative component of MR may be attributed to the decrease of the in-plane spin-dependent scattering. At $T$ = 100 K, a larger MR was also observed in $\rho_{ab}$ and $\rho_c$, which is attributed to the enhanced in-plane and interplane spin correlation, respectively. In particular, the interplane MR is extremely large [$\rho_c(0)/\rho_c(H) \sim 10^4\%$ at 50 kOe] because of the field-induced incoherent-coherent transition for the $c$ axis charge transport at this $T$.

In the low-$T$ case at 4.2 K, $\rho_c$ drastically decreases in the low-field region during the magnetization process, and becomes constant when the M is saturated at $H$ of ~5 kOe. Although a similar $H$ dependence was also observed in the in-plane MR, the interplane MR $\{[\rho_c(0) - \rho_c(H_{sat})]/\rho_c(H_{sat}) \sim 240\%\}$ is much greater than the in-plane MR $\{[\rho_{ab}(0) - \rho_{ab}(H_{sat})]/\rho_{ab}(H_{sat}) \sim 10\%\}$. A considerably larger MR in $\rho_{ab}$ than in $\rho_c$ is reminiscent of the observation of a larger

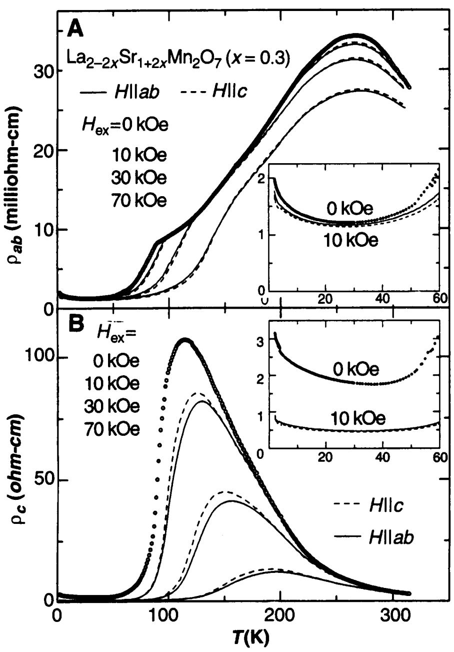


**Fig. 3.** Temperature dependence of (**A**) $\rho_{ab}$ and (**B**) $\rho_c$ under various magnetic fields with different field orientations ($H \parallel c$ and $H \perp c$), in the $La_{2-2x}Sr_{1+2x}Mn_2O_7$ ($x$ = 0.3) crystal. Inset: Expanded view of low-temperature region, which shows the much greater MR effect in $\rho_c$ than in $\rho_{ab}$ at a field of 10 kOe. The axis labels in the main panels also apply to the inset.

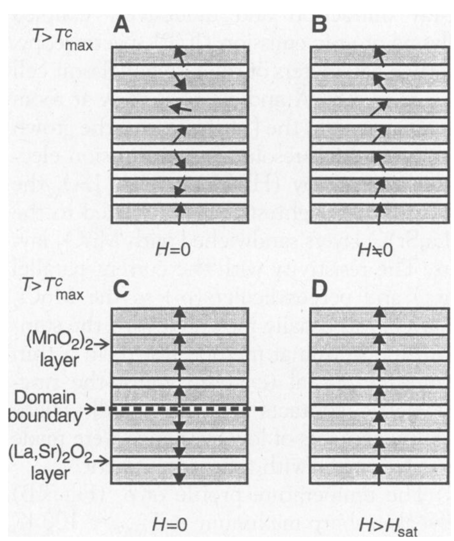


**Fig. 4.** Schematic spin arrangement in $La_{2-2x}Sr_{1+2x}Mn_2O_7$. (**A**) Above the interplane FM ordering temperature $T^{c}_{max}$ (but below $T^{ab}_{max}$), magnetic moments are two dimensionally correlated in a FM moment but thermally disordered among the $MnO_2$ bilayers. (**B**) Magnetic moments rotate toward the direction of a magnetic field under a relatively high field. (**C**) At $T$s sufficiently below $T^{c}_{max}$, magnetic moments within a domain exhibit 3D ordering but some neighboring domains are separated by a domain boundary lying on the $(La,Sr)_2O_2$ layer. (**D**) Application of a field $H > H_{sat}$ aligns all of the magnetic moments and extinguishes the interplane domain boundary as a barrier of the spin-polarized electron tunneling.

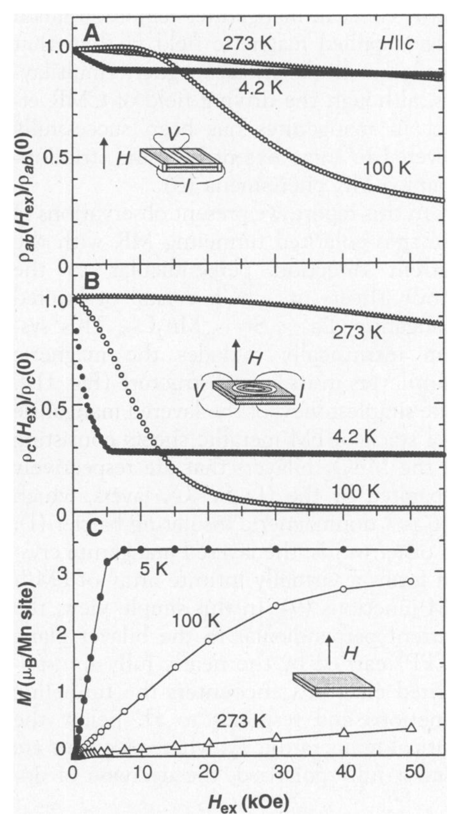


**Fig. 5.** Normalized (**A**) $\rho_{ab}$ and (**B**) $\rho_c$ and (**C**) $M$ as a function of $H$ parallel to the $c$ axis at 4.2, 100, and 273 K for a sample with demagnetizing factor $N/4\pi \approx 0.9$ of the $La_{2-x}Sr_{1+2x}Mn_2O_7$ ($x$ = 0.3) crystal.

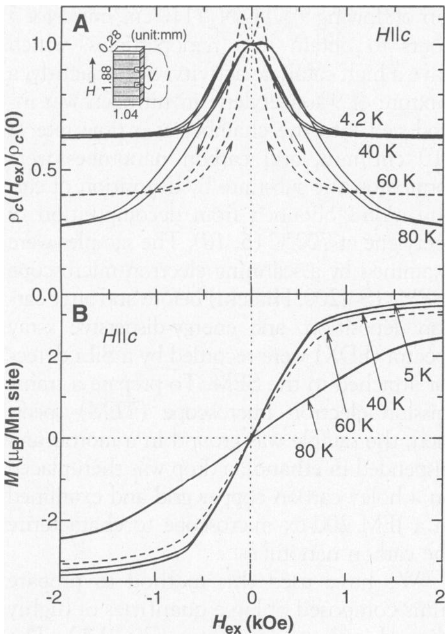


**Fig. 6.** (**A**) Normalized $\rho_c$, and (**B**) $M$ as a function of a $H$ parallel to the $c$ axis at various $T < T^c_{max}$ for a sample with demagnetizing factor $N/4\pi \approx 0.08$ of the $La_{2-x}Sr_{1+2x}Mn_2O_7$ ($x$ = 0.3) crystal.

CPP-MR than current-in-plane (CIP)–MR in artificial magnetic multilayers (*16*). The merit of the perovskite manganites is that the spin polarization $\eta$ of the conduction electrons is very large (reaching 100% at $T \ll T_c$) as compared with the case of conventional FM transition metal [for example, for Ni, $\eta \approx 11\%$ (*17*)]. Therefore, the interplane tunneling probability should be very sensitive to the respective spin states in the adjacent $MnO_2$ bilayers.

In the configuration with $H$ parallel to the $c$ axis ($H \parallel c$), the samples for Figs. 3 and 5 [$\sim 1 \times 1 \times 0.08$ ($c$ axis) mm$^3$] have a large demagnetizing factor [$N/4\pi \approx 0.9$, which was estimated by using the correction for ellipsoids with three different axes (*18*)]. Thus, the real saturation field $H_{sat}$ for this configuration should be much smaller than that presented in Fig. 5. To minimize the demagnetizing effect, we measured both the field dependence of the interplane MR and M for a sample with small demagnetizing factor for $H \parallel c$ [$1.04 \times 0.28 \times 1.88$($c$ axis) mm$^3$, $N/4\pi \approx 0.08$]. Figure 6 displays the results with $H \parallel c$ at several $T$'s below $T^c_{max}$. Below 40 K, the MR is rather insensitive to $T$. Small but clear hystereses were observed in isothermal MR curves, perhaps reflecting a high sensitivity of resistance measurement, though the hysteresis was not clearly discernible in the M curves. With increasing $T$ toward $T^c_{max}$, the saturated resistivity further decreases because of the additional MR effect arising from the field alignment of the thermally fluctuated magnetic domain along the $c$ axis.

The MR ratio $[\rho_c(0) - \rho_c(H_{sat})]/\rho_c(H_{sat})$ could vary from sample to sample, or from electrode to electrode, or both. In our measurements, the ratios were 30 up to 240% at temperatures sufficiently below $T^c_{max}$. Although the origin of the scatter in the data has not been understood yet, a statistical distribution of the interplane magnetic domain boundaries might be responsible. $H_{sat}$, which appears around 1 kOe in the sample for Fig. 6, will be ~400 Oe when the demagnetization effect is properly corrected.

We have presented the interplane tunneling MR in a layered manganite crystal, $La_{2-2x}Sr_{1+2x}Mn_2O_7$ ($x$ = 0.3), which is viewed as composed of FM-metallic $MnO_2$ bilayers with intervening nonmagnetic insulating $(La,Sr)_2O_2$ blocks. In the 2D FM region, $T^c_{max}$ (~100 K) $\le T \le T^{ab}_{max}$ (~270 K), the field-induced incoherent-coherent transition for the interplane ($c$ axis) charge transport contributes mostly to the extremely large MR effect. Even below the interplane spin-ordering temperature $T^c_{max}$, the interplane tunneling of the almost fully spin-polarized electrons is blocked at the interplane magnetic domain boundaries on the insulating $(La,Sr)_2O_2$ layers, but is recovered during the magnetization process. This field-sensitive tunneling process gives rise to a low-field (<1 kOe) MR as large as ≥200%. The layered manganite thus intrinsically contains the infinite arrays of FM/I/FM junctions in its crystal structure, and shows a colossal interplane tunneling MR.


## REFERENCES AND NOTES

1. M. N. Baibich *et al.*, *Phys. Rev. Lett.* **61**, 2472 (1988).
2. S. S. P. Parkin, Z. G. Li, D. J. Smith, *Appl. Phy. Lett.* **58**, 2710 (1991).
3. A. E. Berkowitz *et al.*, *Phys. Rev. Lett.* **68**, 3745 (1992); J. Q. Xiao, J. S. Jiang, C. L. Chien, *ibid.*, p. 3749.
4. B. Dieny *et al.*, *Phys. Rev. B* **43**, 1297 (1991).
5. T. Miyazaki and N. Tezuka, *J. Magn. Magn. Mater.* **139**, L231 (1995).
6. For example, K. Chahara, T. Ohno, M. Kasai, Y. Kozono, *Appl. Phys. Lett.* **63**, 1990 (1993); S. Jin *et al.*, *Science* **264**, 413 (1994).
7. C. Zener, *Phys. Rev.* **82**, 403 (1951); P. W. Anderson and H. Hasegawa, *ibid.* **100**, 675 (1955); P.-G. de Gennes, *ibid.* **118**, 141 (1960); K. Kubo and N. Ohta, *J. Phys. Soc. Jpn.* **33**, 21 (1972).
8. H. Kuwahara *et al.*, *Science* **272**, 80 (1996).
9. M. Julliere, *Phys. Lett. A* **54**, 225 (1975); S. Maekawa and U. Gefvert, *IEEE Trans. Magn.* **18**, 707 (1982).
10. Y. Moritomo, A. Asamitsu, H. Kuwahara, Y. Tokura, *Nature* **380**, 141 (1996).
11. Y. Tomioka, A. Asamitsu, H. Kuwahara, Y. Moritomo, Y. Tokura, *Phys. Rev. B* **53**, R1689 (1996).
12. Y. Okimoto *et al.*, *Phys. Rev. Lett.* **75**, 109 (1995).
13. Y. Maeno *et al.*, *Nature* **372**, 532 (1994).
14. For example, S. L. Cooper and K. E. Gray, in *Physical Properties of High Temperature Superconductors IV*, D. M. Ginsberg, Ed. (World Scientific, Singapore, 1994), chap. 3.
15. T. G. Perring, G. Aeppli, Y. Moritomo, Y. Tokura, preprint.
16. M. A. M. Gijs, S. K. J. Lenczowski, J. B. Giesbers, *Phys. Rev. Lett.* **70**, 3343 (1993).
17. P. M. Tedrow and R. Meservey, *Phys. Rev. B* **7**, 318 (1973).
18. J. A. Osborn, *Phys. Rev.* **67**, 351 (1945).


19. We thank G. Aeppli, Y. Moritomo, R. Kumai, M. Kasai, and B. Raveau for helpful discussions. This work, supported in part by NEDO, was performed in JRCAT under the joint research agreement between NAIR and ATP.

16 August 1996; accepted 17 October 1996


# Large-Scale Synthesis of Aligned Carbon Nanotubes

W. Z. Li, S. S. Xie,* L. X. Qian, B. H. Chang, B. S. Zou, W. Y. Zhou, R. A. Zhao, G. Wang

**Large-scale synthesis of aligned carbon nanotubes was achieved by using a method based on chemical vapor deposition catalyzed by iron nanoparticles embedded in mesoporous silica. Scanning electron microscope images show that the nanotubes are approximately perpendicular to the surface of the silica and form an aligned array of isolated tubes with spacings between the tubes of about 100 nanometers. The tubes are up to about 50 micrometers long and well graphitized. The growth direction of the nanotubes may be controlled by the pores from which the nanotubes grow.**

The discovery of carbon nanotubes (*1*) has led to much speculation about their properties and potential applications (*2*). Large quantities of carbon nanotubes can now be produced by either arc discharge (*3*, *4*) or thermal deposition of hydrocarbons (*5*, *6*). However, experimental characterizations and applications of the nanotubes have been hampered because of problems with the alignment of the nanotubes.

Recently, Ajayan *et al.* (*7*) developed a simple method to produce aligned arrays of carbon nanotubes by cutting a polymer resin-

W. Z. Li, S. S. Xie, B. H. Chang, B. S. Zou, W. Y. Zhou, R. A. Zhao, G. Wang, Institute of Physics, Chinese Academy of Sciences, Beijing 100080, China.
L. X. Qian, Department of Physics, Central University of Nationalities, Beijing 100081, China.

*To whom correspondence should be addressed. E-mail: user412@aphy01.iphy.ac.cn